Supporting Information

Resilient ion/electron dual conductive network via covalent/hydrogen bond cross-linking enable stable and high-energy-density Si-C anodes in Lithium-ion batteries

Yupeng Xiao[a,b], Tianle Li[a,b], Xiaoqian Hao[a,b], Tianjiao Zhu[a,b], Jingqi Zang[a,b], Yuqian Li[a,b], Wenju Wang[a,b,*]

[a] School of Energy and Power Engineering, Nanjing University of Science and Technology, Nanjing 210094, P. R. China

[b] Energy and Technology Institute, Nanjing University of Science and Technology, Nanjing 210094, P. R. China

E-mail: ypxiao@njust.edu.cn; wangwenju@njust.edu.cn

Table S1. The components of Si-C and NCM811 electrodes in this work.

Electrodes	Binder	Conductive agent	Si-C Mass loading （mg cm^{-2}）	Mass ratio (active material: conductive agent: binder)
Si-C/LPC	LiPAA	c-CNT	1.2-2.2	90:5:5
Si-C/CSC	c-CS	c-CNT	1.2-2.2	90:5:5
Si-C/LPCC	LPCS (mixture of LiPAA and c-CS)	c-CNT	1.2-2.2	90:5:5
Si-C/LPCS	LPCS	Carbon black	~1.2	90:5:5
Si-C/PCC	PCS (mixture of PAA and c-CS)	c-CNT	~1.2	90:5:5
Si/LPCC	LPCS	c-CNT	0.7-7.5	96:2:2
NCM811	PVDF	Carbon black	19.5 mg cm^{-2}	94:4:2

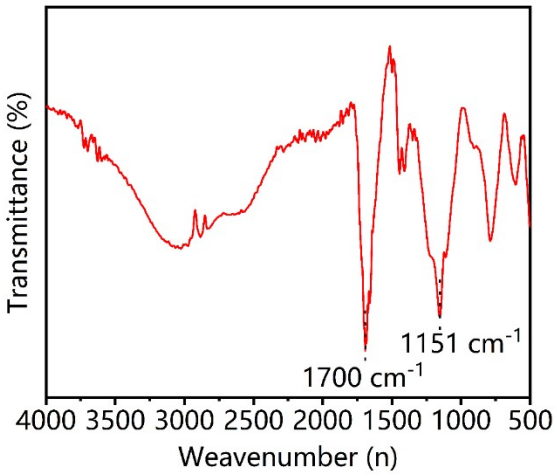

Fig. S1. FT-IR spectra of PAA.

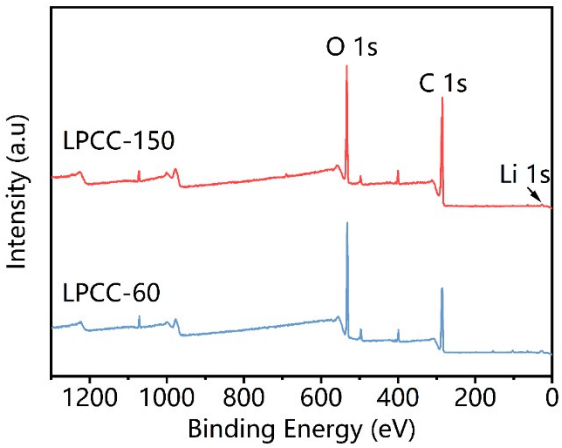

Fig. S2 XPS survey spectra of as-prepared binders.

Table S2. XPS elemental compositions of LPCC-60 and LPCC-150.

Element	LPCC-60 (at%)	LPCC-150 (at%)
C	56.6	68.1
Li	8.8	4.4
N	4.7	4.3
O	29.9	23.2

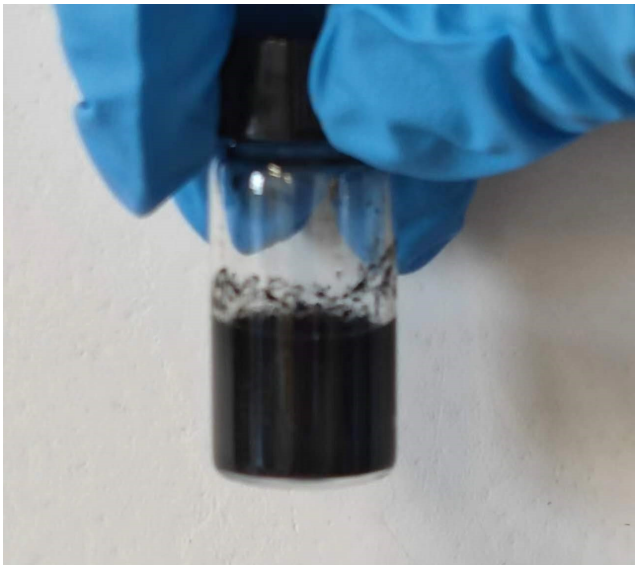

Fig. S3. Photos of LPCC solutions

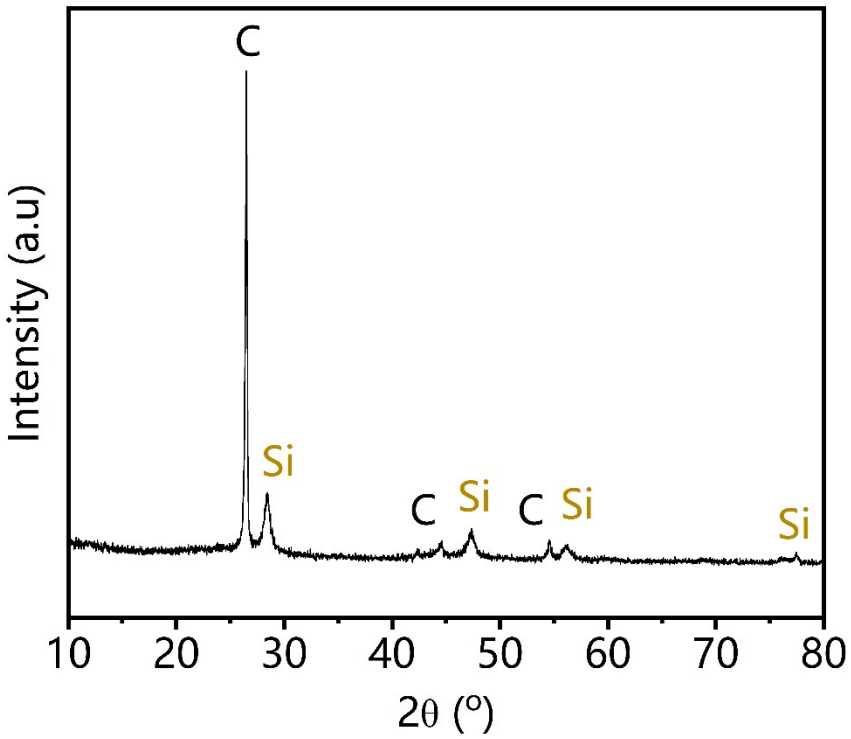

Fig. S4. XRD patterns of Si-C anodes.

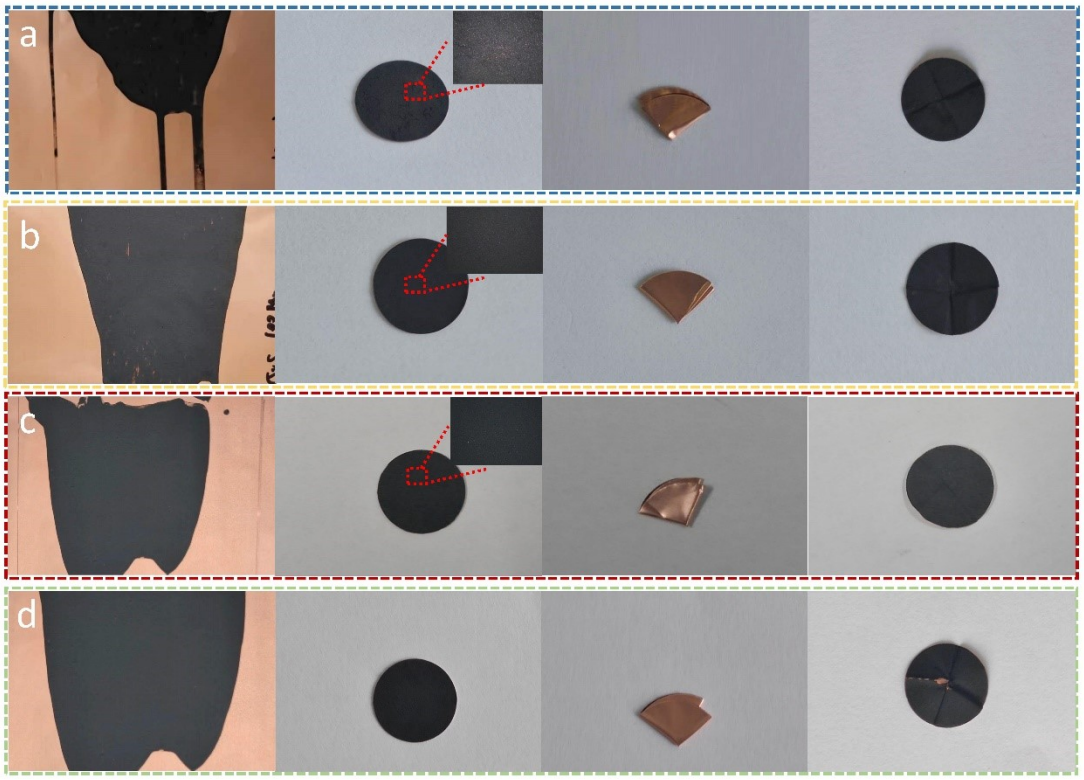

Fig. S5. Photos of electrodes after three times fold, and their corresponding unfolded states

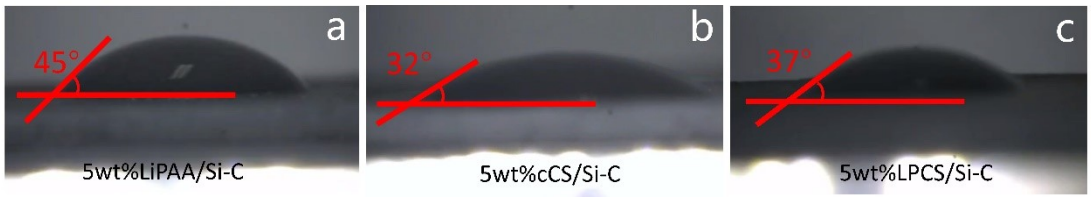

Fig. S6. The contact angles of a) LiPAA, b) c-CS, and c) LPCS solution on Si-C composite.

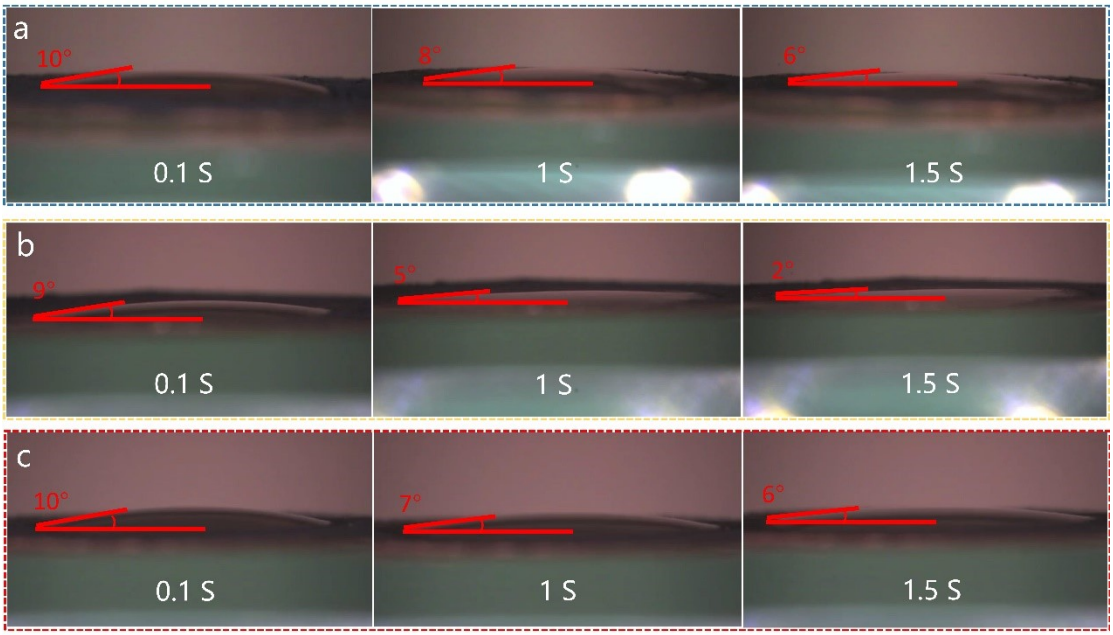

Fig. S7. The contact angles of electrolyte on a) Si-C/LPC, b) Si-C/CSC, and c) Si-C/LPCC electrodes.

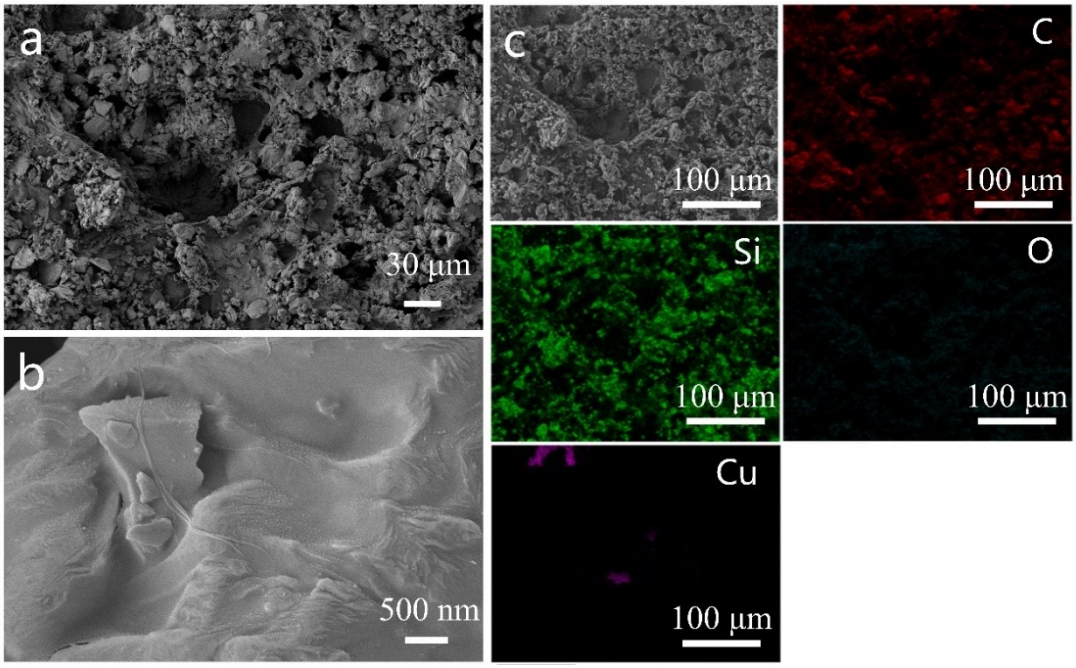

Fig. S8. The SEM images and corresponding element maps of Si-C/LPC electrode.

Table S3 EDS elemental composition of Si-C/LPC electrode.

Elements	Content (at%)
C	81.41
Si	7.53
O	10.74
Cu	0.32

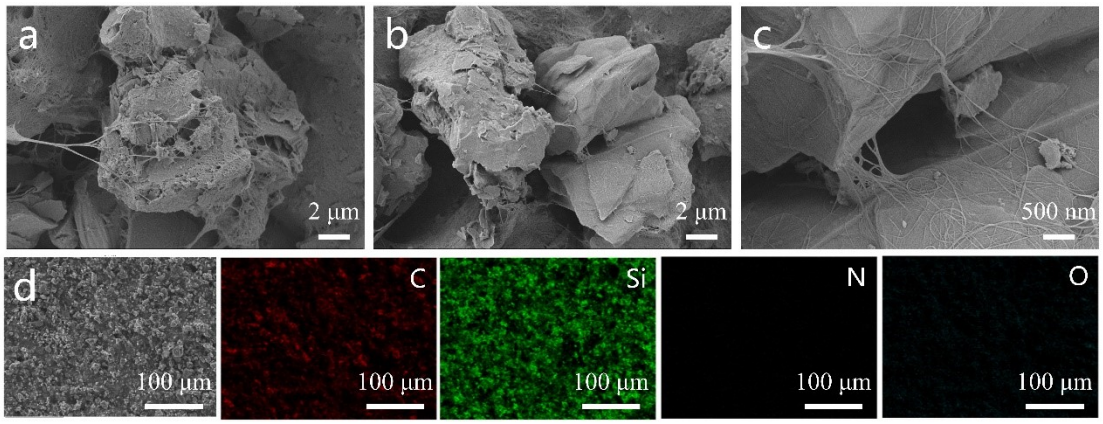

Fig. S9. The SEM images and corresponding element maps of Si-C/CSC electrode.

Table S4 EDS elemental composition of Si-C/CSC electrode.

Elements	Content (at%)
C	82.35
Si	8.84
O	8.27
N	0.55

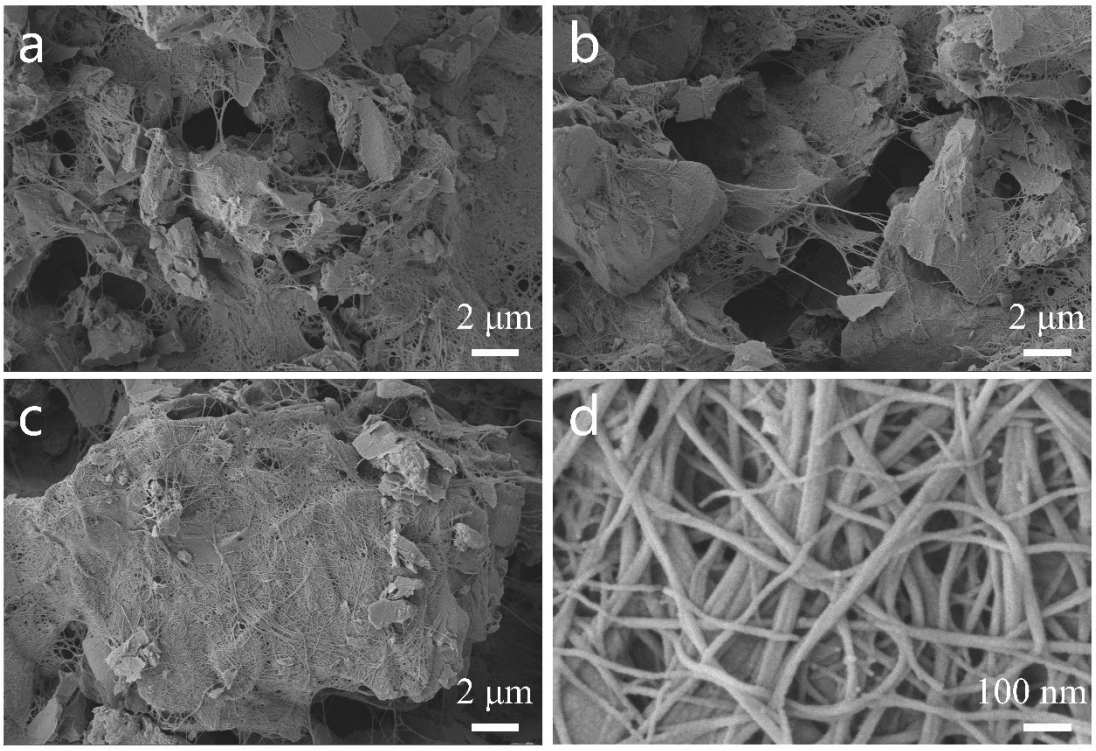

Fig. S10. The SEM images of Si-C/LPC electrode.

Table S5. EDS elemental composition of Si-C/LPCC electrode.

Elements	Content (at%)
C	83.40
Si	8.65
O	7.57
N	0.38

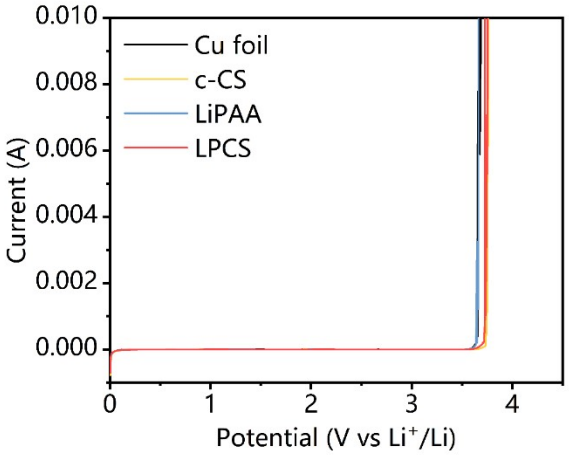

Fig. S11. LSV curves of different polymeric films with the voltage range of 0.005-4 V with a scan rate of 0.2 mV s^{-1}.

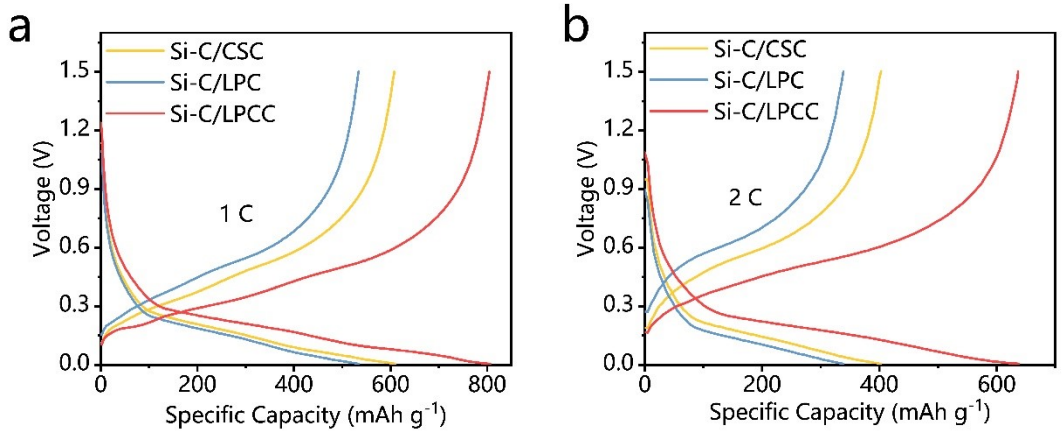

Fig. S12. Galvanostic charge/discharge profiles of Si-C/CSC, Si-C/CSC, and Si-C/LPCC at current density of a) 1C, and b) 2C.

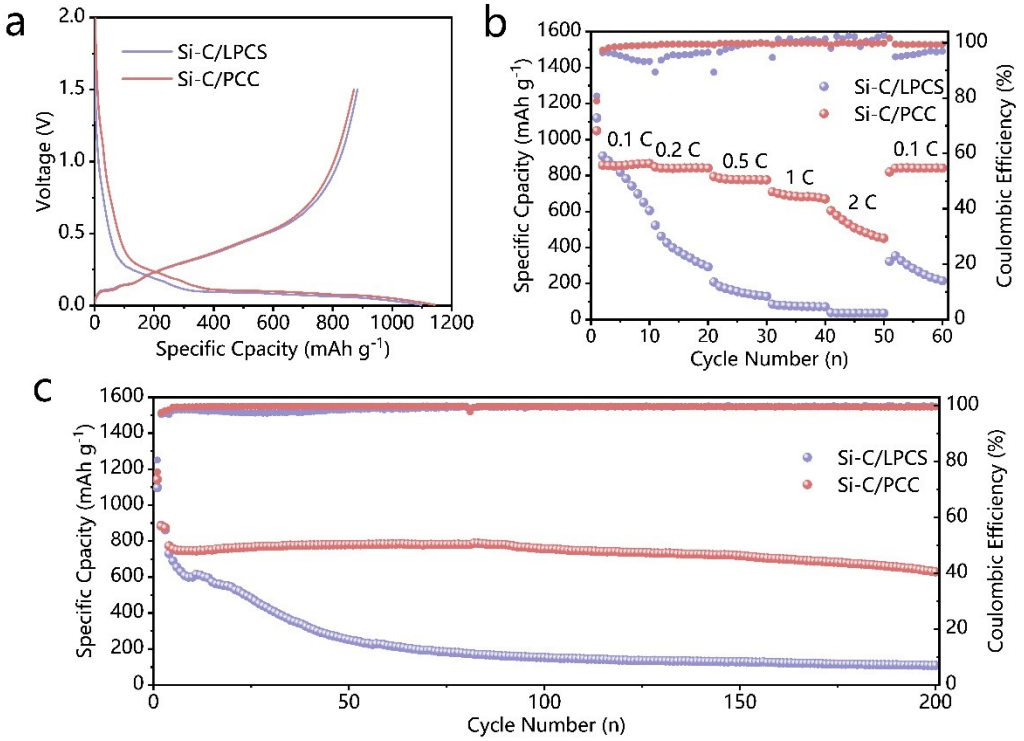

Fig. S13. Electrochemical performance of Si-C/LPCS and Si-C/PCC electrodes. a) Initial galvanostatic charge and discharge profiles. b) Rate performance. c) Cycling performance at 0.5C.

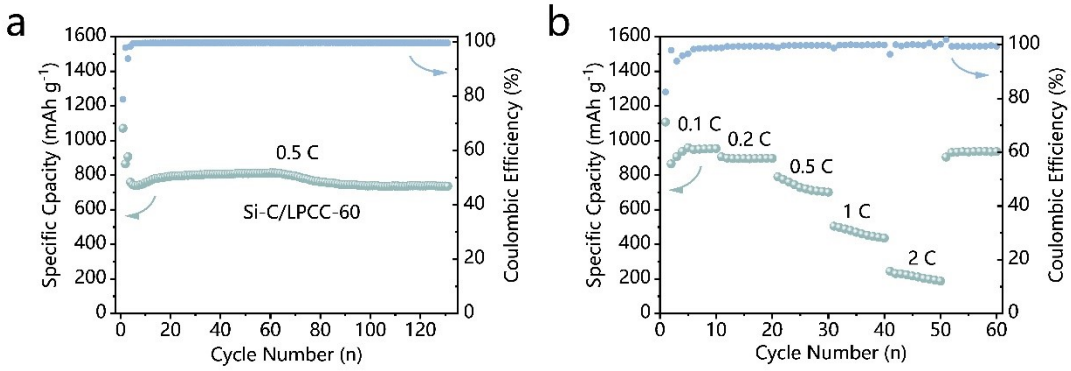

Fig. S14. Electrochemical performance of Si-C/LPCC-60.

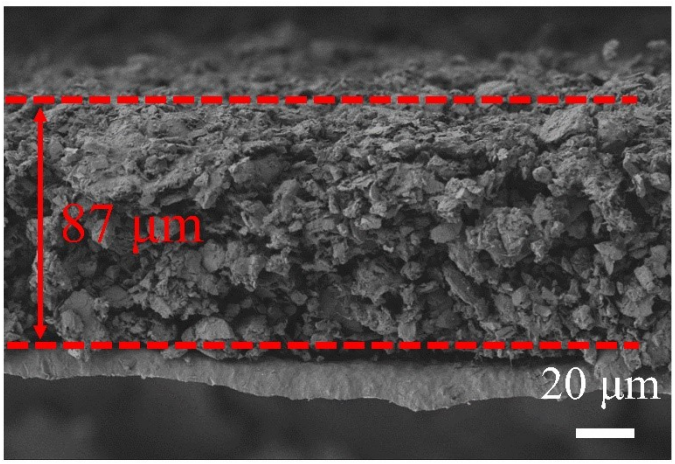

Fig. S15. The cross-sectional SEM images of Si-C/LPCC electrodes with Si-C mass loading of 7.5 mg cm^{-2}.

Table S6. Comparison of active material content and areal capacity between Si-C/LPCC electrode and previously advanced Si-based electrodes.

	Mass loading (mg cm^{-2})	Areal capacity (mAh cm^{-2})	Active material content (wt%)	Current density	Capacity retention/ cycle number	References
Si-C/LPCS	7.5	6.6	96	0.2C	98%@30	This work
Si-C/PAHT	4-6	4	90	0.1C	89%@100	[1]
Si-C/APA-CNT	15	7.79	80	0.2 A g^{-1}	~80%@60	[2]
Si-C/PSEA	5	4	80	0.1C	92%@120	[3]
Si-C/TCB	2.03	~2.6	80	0.5C	82%@150	[4]
Si-C/CA-PAA	3	3	80	0.1C	90%@100	[5]
Si-C/XG	1.82	4.75	60	0.4 A g^{-1}	47%@50	[6]
Si-C/CMC-co-SN	2.5-3	~3	70	0.84 A g^{-1}	-@300	[7]
Si-C/PBDT	1.3	~1.2	80	0.2C	64@300	[8]
Si-C/PAA-SF	0.27	0.84	60	0.5C	~45@500	[9]
Si-C/OXP-CNT-1.5	1.5	~0.9	80	0.2 A g^{-1}	73.8@100	[10]
Si-C/Alg-g-PAMA	1.2	~1.3	76	0.5C	~65@200	[11]

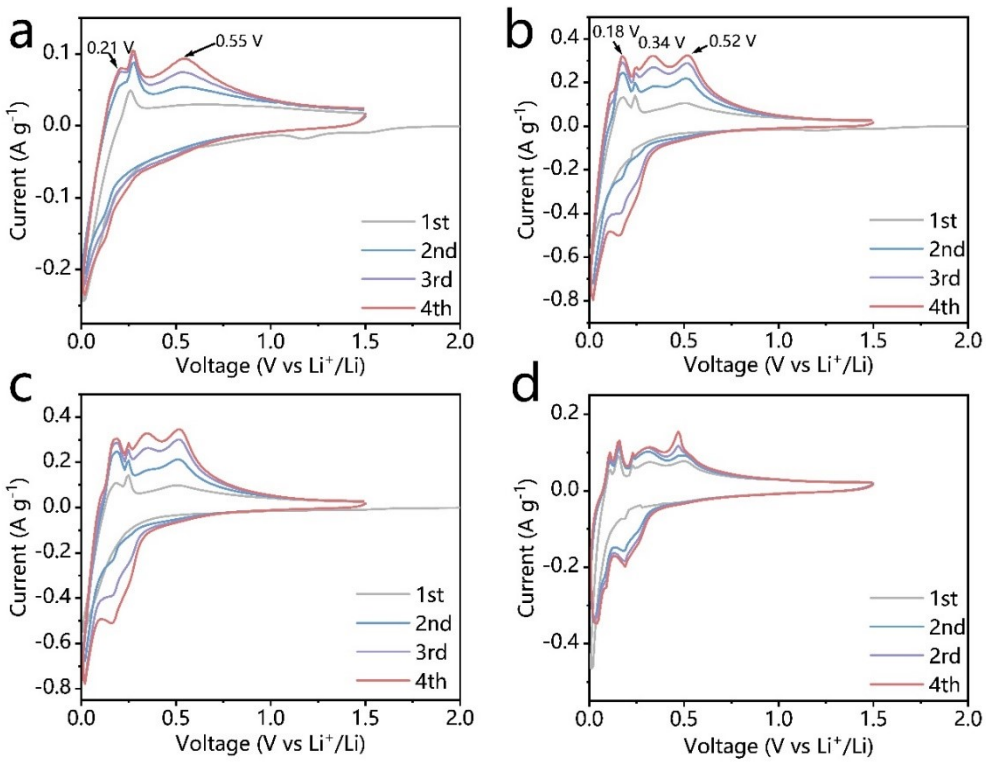

Fig. S16. CV curves of a) Si-C/CSC, b) Si-C/LPC, c) Si-C/LPCS, and d) Si-C/PCC.

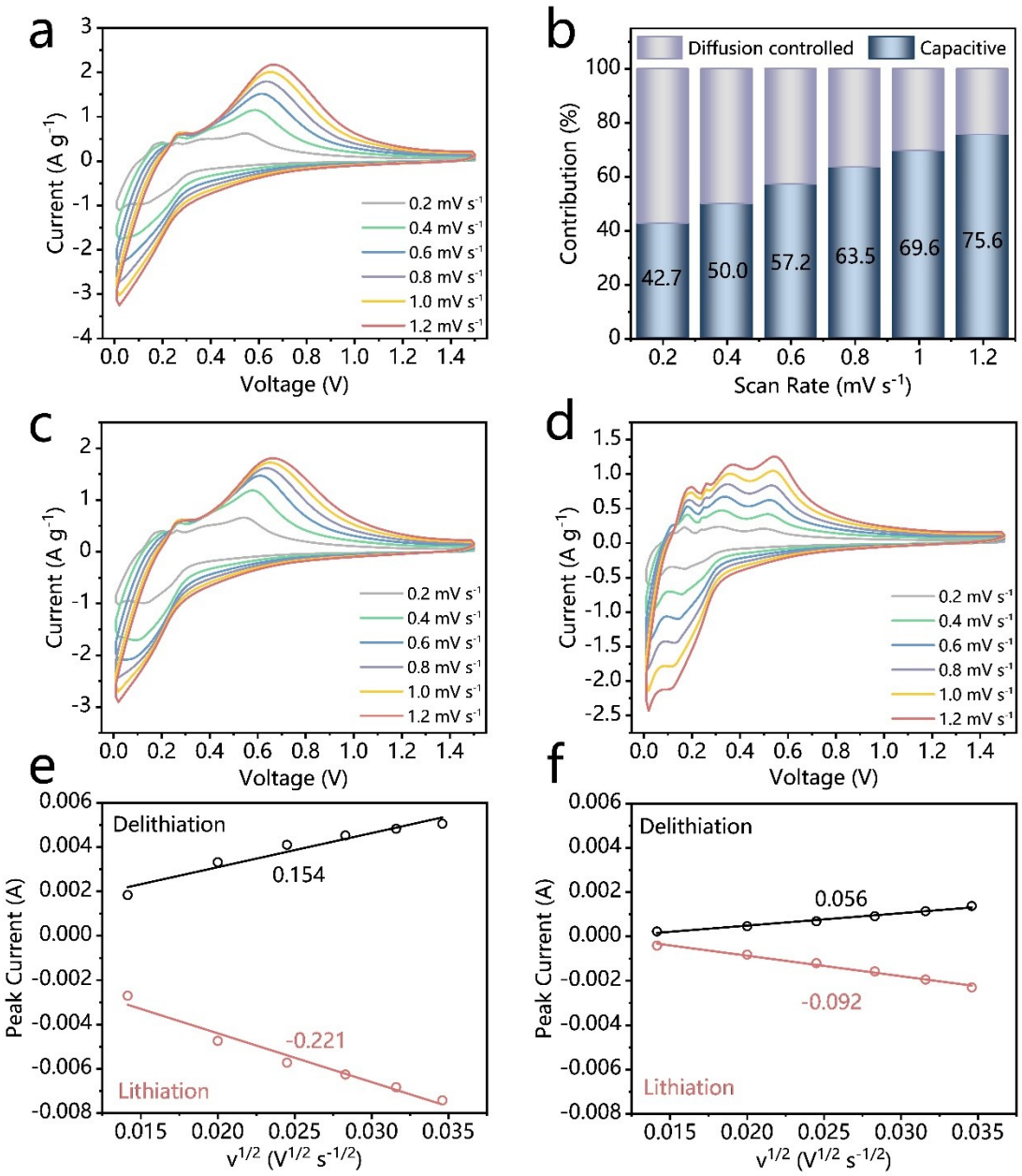

Fig. S17. CV curves at different scan rates from 0.2 to 1.2 mV s^{-1} of a) Si-C/CSC electrode and b) corresponding ratio of diffusion and capacitance contributions at different scan rates. c) CV curves of Si-C/LPCS electrode and e) corresponding relationship between scan rate and peak current. d) Si-C/PCC electrode and f) corresponding relationship between scan rate and peak current.

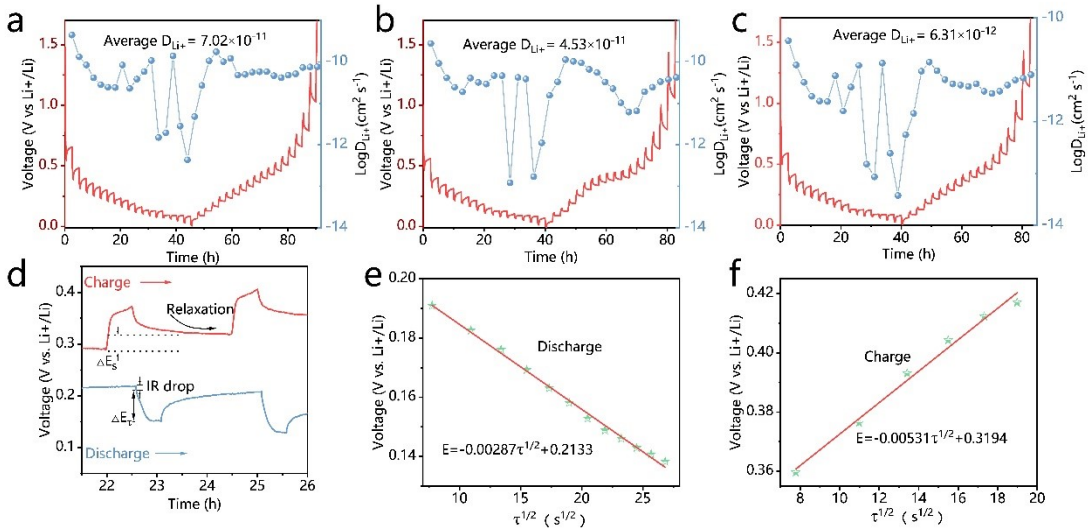

Fig. S18. Transient voltage profiles of a) Si-C/LPC, b) Si-C/LPCS, c) Si-C/PCC based on GITT for the diffusion-dependent electrodes and d) partial zoom-in curves of Transient voltage profiles. Variation of the potential against $\tau^{1/2}$ during e) discharge and f) charge.

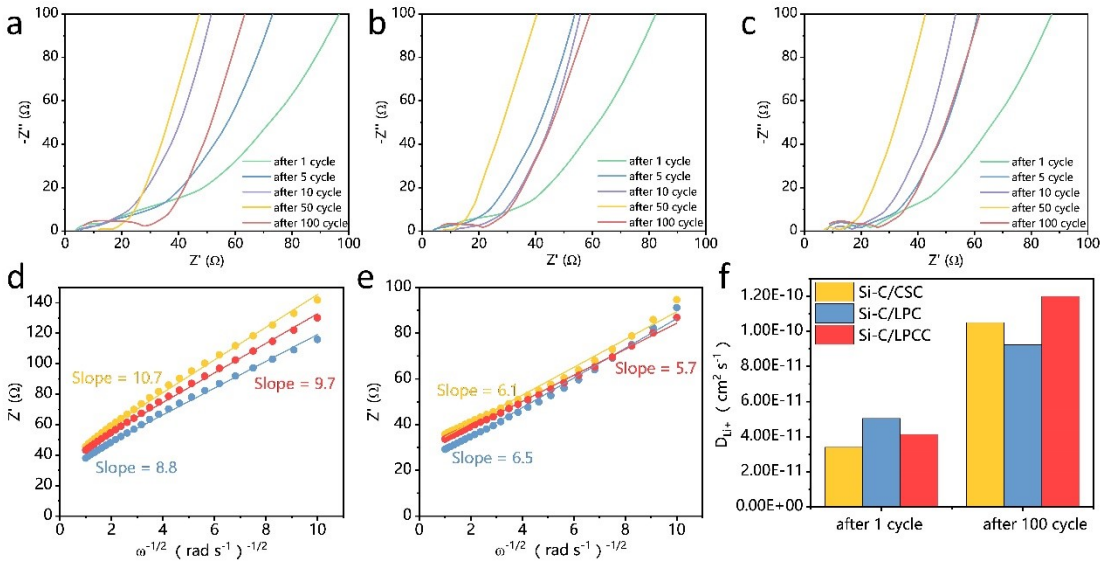

Fig. S19. The electrochemical impedance spectra at 1, 5, 10, 50 and 100 cycles for a) Si-C/CSC, b) Si-C/LPC, and c) Si-C/LPCC. The kinetics calculations based on the frequency (W) and Z' values at low frequency region at d) 1 cycle and e) 100 cycles. f) Corresponding Li^+ diffusion coefficient.

The Li^+ diffusion coefficients could be calculated according to the Equation:

$$D = (R^2T^2) / (2A^2n^4F^4C^2\sigma^2)$$

Where D is the Li^+ diffusion coefficients, R is the gas constant, T is the absolute temperature, A is the surface area of anode, *n* is the number of electrons per molecule during reaction, F is the Faraday constant, C is the concentration of Li^+. The Warburg factor (σ) was carried out from the slop in fitting line of $\omega^{-1/2}$ and Z' according to Equation:

$$Z' = R_e + R_{ct} + \sigma\omega^{-1/2}$$

Where R_e represents the resistance between electrode and electrolyte, and R_{ct} is charge transfer resistance.

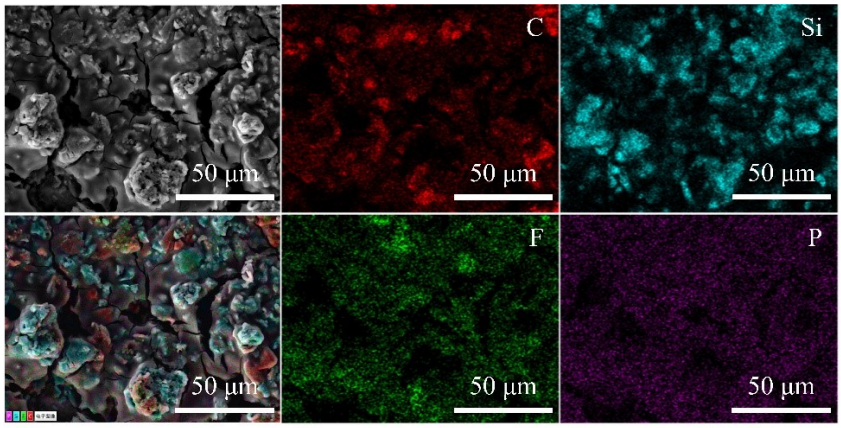

Fig. S20. The SEM images and corresponding element maps of Si-C/LPC electrode after 100 cycles.

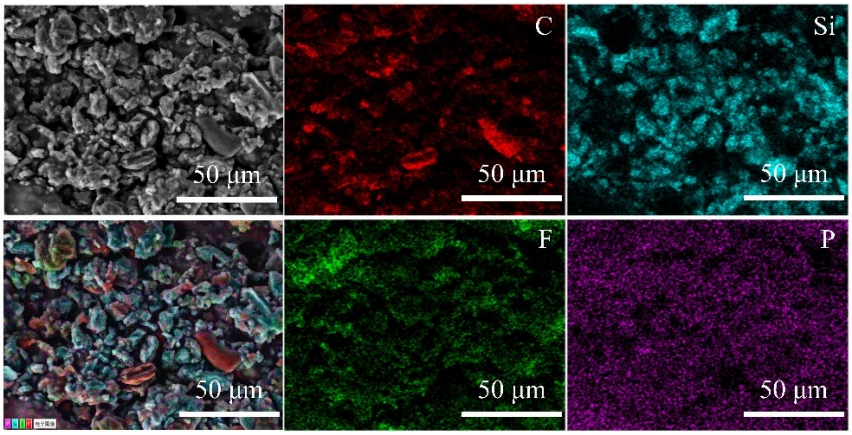

Fig. S21. The SEM images and corresponding element maps of Si-C/CSC electrode after 100 cycles.

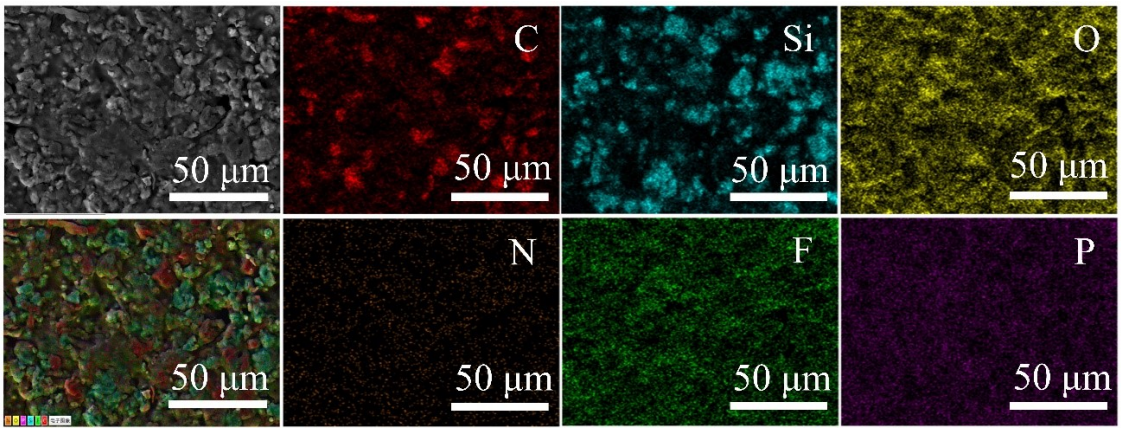

Fig. S22. The SEM images and corresponding element maps of Si-C/LPCC electrode after 100 cycles.

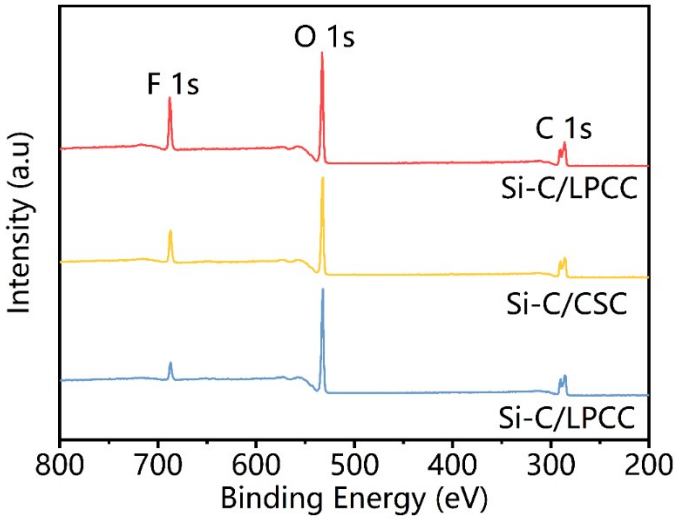

Fig. 23. XPS survey spectra of Si-C/LPC, Si-C/CSC, and Si-C/LPCC electrodes after 100 cycles at 0.2 C.

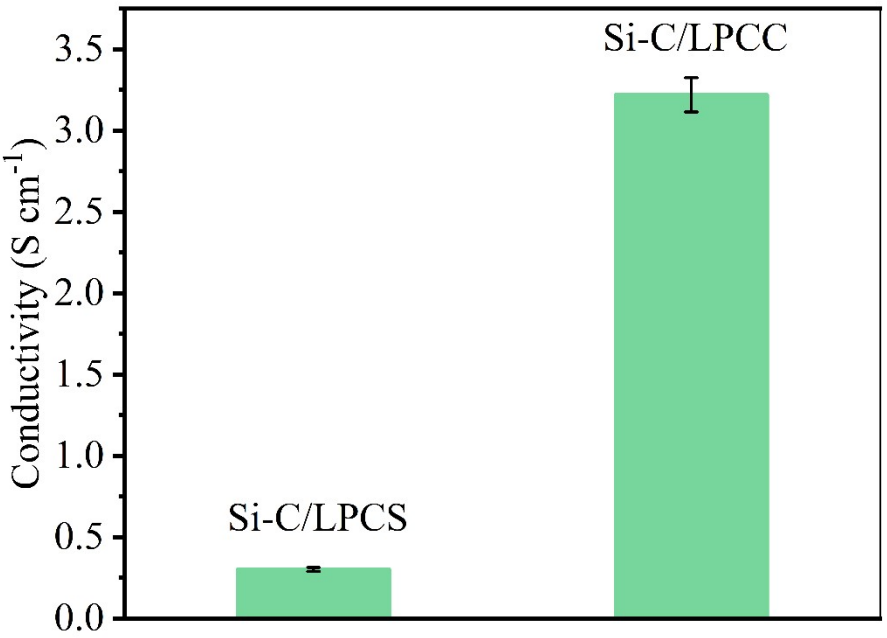

Fig. S24. The conductivity of Si-C/LPCS and Si-C/LPCC electrodes.

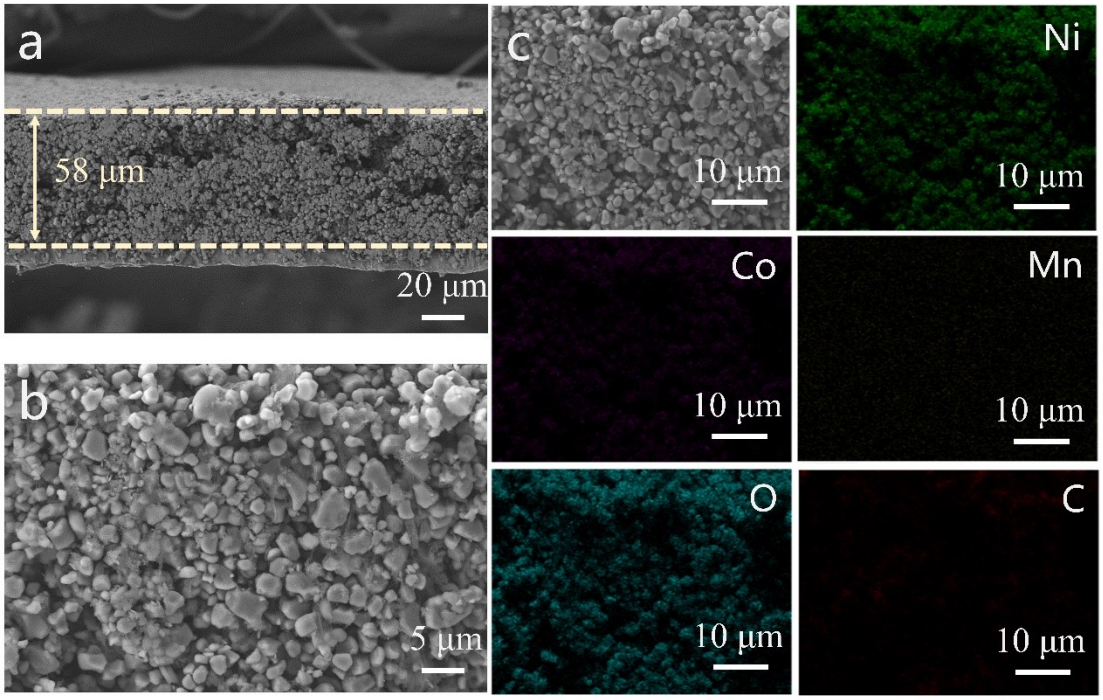

Fig. S25. Cross-sectional SEM images and corresponding element maps of high-mass-loading NCM811 cathodes (19.5 mg cm^{-2}).

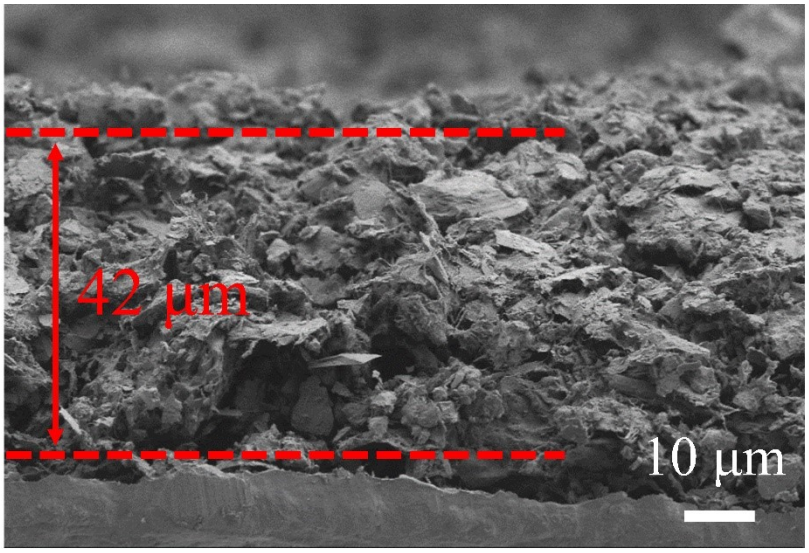

Fig. S26. Cross-sectional SEM images Si-C anodes with a mass loading of 3.5 mg cm^{-2}.

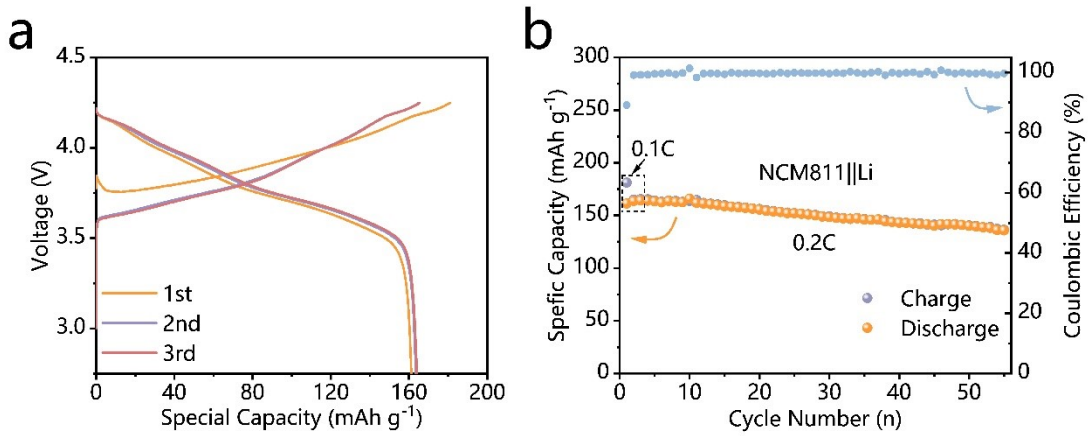

Fig. S27. Electrochemical performance of NCM||Li half-cell. a) The first three charge/discharge profiles and b) Cycling performance.

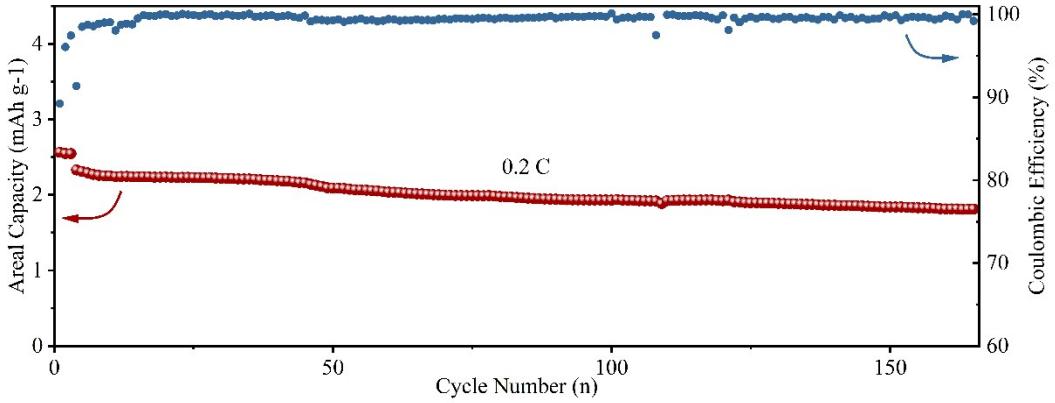

Fig. S28. Plots of cycle number versus specific capacity for NCM||Si-C/LPCC full-cell with the mass loading of NCM811 at10.8 mg cm^{-2}.

Table S7. Cell parameters for calculating gravimetric and volumetric energy density of each samples, and the comparison of gravimetric and volumetric energy density of our full cells with previosuly reported full cells

Anode electrode information for full-cell

	Mass loading (mg cm^{-2})	Active material content (%)	Electrode thickness (μm)	references
Si-C/LPCS	3.5	96	42	This work
EGS	3.4	85	31	[12]
F-Si|E-GEL	1.4	60	40	[13]
VGSs/C@Si-C	2.0	80	35	[14]
SGC-19/Gr	—	94	52	[15]
SiO_xC_y	6.3	80	~60	[16]
SiOx@Gr	6.7	93.5		[17]
C/Si@MPC-G	6.33	95	39.5	[18]

Cathode electrode information for full-cell

	Mass loading (mg cm^{-2})	Active material content (%)	Electrode thickness (μm)	references
Si-C/LPCS	19.5	94	58	This work
EGS	21	96	54	[12]
F-Si|E-GEL	17-18	96	60	[13]
VGSs/C@Si-C	15,.6	84	49	[14]
SGC-19/Gr	—	96.5		[15]
SiO_xC_y	26.5	80	~50	[16]
SiOx@Gr	25	96		[17]
C/Si@MPC-G	20.8	96	57.9	[18]

Table S8. Comparison of gravimetric and volumetric energy density of our full cells with recently reported full cells

	gravimetric energy density (Wh kg^{-1})	volumetric energy density (Wh L^{-1})	references
Si-C/LPCS	510	1172	This work
EGS	345	623	[12]
F-Si|E-GEL	413	1022	[13]
VGSs/C@Si-C	311	1008.2	[14]
SGC-19/Gr	382	960	[15]
SiO_xC_y	355	1020	[16]
SiOx@Gr	420	449	[17]
C/Si@MPC-G	333	932	[18]
Si/G	474	912	[19]

References

[1] L. Hu, X. Zhang, P. Zhao, H. Fan, Z. Zhang, J. Deng, G. Ungar, J. Song, Gradient H-Bonding Binder Enables Stable High-Areal-Capacity Si-Based Anodes in Pouch Cells, Advanced Materials 33 (2021) 2104416.

[2] F. Zhang, H. Xia, T. Wei, H. Li, M. Yang, A.-M. Cao, A new universal aqueous conductive binder via esterification reinforced electrostatic/H-bonded self-assembly for high areal capacity and stable lithium-ion batteries, Energy & Environmental Science 17 (2024) 238-248.

[3] L. Hu, M. Jin, Z. Zhang, H. Chen, F. Boorboor Ajdari, J. Song, Interface-Adaptive Binder Enabled by Supramolecular Interactions for High-Capacity Si/C Composite Anodes in Lithium-Ion Batteries, Advanced Functional Materials 32 (2022) 2111560.

[4] X. Lin, Y. Wen, J. Wang, S. Wang, X. Sun, H. Liu, X. Xu, Co-operation of hydrogen bonds and dynamic covalent bonds enables an energy-dissipative crosslinked binder for silicon-based anodes, Green Chemistry 26 (2024) 2078-2086.

[5] Y. Wang, H. Xu, X. Chen, H. Jin, J. Wang, Novel constructive self-healing binder for silicon anodes with high mass loading in lithium-ion batteries, Energy Storage Materials 38 (2021) 121-129.

[6] E. Zhao, Z. Guo, J. Liu, Q. Zhang, Z. Guo, Y. Yang, H. Wang, L. Wang, A low-cost and eco-friendly network binder coupling stiffness and softness for high-performance Li-ion batteries, Electrochimica Acta 387 (2021) 138491.

[7] W.-F. Ren, J.-B. Le, J.-T. Li, Y.-Y. Hu, S.-Y. Pan, L. Deng, Y. Zhou, L. Huang, S.-G. Sun, Improving the Electrochemical Property of Silicon Anodes through Hydrogen-Bonding Cross-Linked Thiourea-Based Polymeric Binders, ACS Applied Materials & Interfaces 13 (2021) 639-649.

[8] J. Zhang, J. Sun, Y. Zhao, Y. Su, X. Meng, L. Yan, T. Ma, Prelithiated rigid polymer with high ionic

conductivity as silicon-based anode binder for lithium-ion battery, Journal of Colloid and Interface Science 649 (2023) 977-985.
[9] P. Dong, X. Zhang, J. Zamora, J. McCloy, M.-K. Song, Silk fibroin-based biopolymer composite binders with gradient binding energy and strong adhesion force for high-performance micro-sized silicon anodes, Journal of Energy Chemistry 80 (2023) 442-451.
[10] F. Zhang, H. Xia, T. Wei, B. Liu, H. Li, Z. Lu, M. Yang, Rotatable Methylene Ether Bridge Units Enabling High Chain Flexibility and Rapid Ionic Transport in a New Universal Aqueous Conductive Binder, Advanced Functional Materials 33 (2023) 2303339.
[11] B. Gendensuren, N. Sugartseren, M. Kim, E.-S. Oh, Incorporation of aniline tetramer into alginate-grafted-polyacrylamide as polymeric binder for high-capacity silicon/graphite anodes, Chemical Engineering Journal 433 (2022) 133553.
[12] J. Ma, J. Sung, Y. Lee, Y. Son, S. Chae, N. Kim, S.-H. Choi, J. Cho, Strategic Pore Architecture for Accommodating Volume Change from High Si Content in Lithium-Ion Battery Anodes, Advanced Energy Materials 10 (2020) 1903400.
[13] M. Je, H.B. Son, Y.-J. Han, H. Jang, S. Kim, D. kim, J. Kang, J.-H. Jeong, C. Hwang, G. Song, H.-K. Song, T.S. Ha, S. Park, Formulating Electron Beam-Induced Covalent Linkages for Stable and High-Energy-Density Silicon Microparticle Anode, Advanced Science 11 (2024) 2305298.
[14] M. Han, Y. Mu, L. Wei, L. Zeng, T. Zhao, Multilevel carbon architecture of subnanoscopic silicon for fast-charging high-energy-density lithium-ion batteries, Carbon Energy 6 (2024) e377.
[15] R. Fu, J. Ji, L. Yun, Y. Jiang, J. Zhang, X. Zhou, Z. Liu, Graphene wrapped silicon suboxides anodes with suppressed Li-uptake behavior enabled superior cycling stability, Energy Storage Materials 35 (2021) 317-326.
[16] S. Fan, S. Cui, J. Zhang, J. Rong, W. Wang, X. Xing, Y. Liu, W. Ma, J.-T. Zhao, Two Birds with One Stone: Micro/Nanostructured SiOxCy Composites for Stable Li-Ion and Li Metal Anodes, Small 19 (2023) 2304290.
[17] J. Zhao, Z. Shi, Z. He, Z. Zhou, F. Li, M. Su, Y. Zeng, Q. Gu, Y. Li, T. Li, B. Qiu, Z. Liu, Optimizing the potential of intercalation on anode for long-cycle 420 Wh/kg Li-ion batteries, Journal of Power Sources 580 (2023) 233393.
[18] Y. Son, N. Kim, T. Lee, Y. Lee, J. Ma, S. Chae, J. Sung, H. Cha, Y. Yoo, J. Cho, Calendering-Compatible Macroporous Architecture for Silicon–Graphite Composite toward High-Energy Lithium-Ion Batteries, Advanced Materials 32 (2020) 2003286.
[19] Y. Son, T. Lee, B. Wen, J. Ma, C. Jo, Y.-G. Cho, A. Boies, J. Cho, M. De Volder, High energy density anodes using hybrid Li intercalation and plating mechanisms on natural graphite, Energy & Environmental Science 13 (2020) 3723-3731.